Geophysical Journal International

Geophys. J. Int. (2020) **220,** 1095–1111
Advance Access publication 2019 November 05
GJI General Geophysical Methods

doi: 10.1093/gji/ggz505

Fault dip variations related to elastic layering

M. Nespoli, M.E. Belardinelli and M. Bonafede

Department of Physics and Astronomy, University of Bologna, Bologna, Italy. E-mail: massimo.nespoli2@unibo.it

Accepted 2019 November 2. Received 2019 October 31; in original form 2019 May 3

SUMMARY

In this paper, we model the crack growth in an elastic medium constituted by two welded half-spaces with different rigidities. We implement a 2-D boundary element method (BEM) computing shear and normal tractions acting on the crack and the slip accommodating stress drop from an arbitrary initial configuration to a final frictional configuration. The direction of crack growth follows the criterion of maximum energy release (strain and gravitational energy) provided that it overcomes the surface fracture energy and the work dissipated by friction. The energetic criterion leads to estimates of the dip angle of seismic faults depending on the amplitude of the initial stress and it includes the classical Anderson's results as a particular case. Moreover, in presence of a sharp rigidity contrast, the direction of crack growth is strongly deflected. The model simulates non-planar, complex, fault geometries, as in the case of detachment and listric faults and it explains the increase of dip angles for both normal and reverse faults, when they enter soft sedimentary layers.

Key words: Friction; Numerical modelling; Dynamics and mechanics of faulting; Mechanics, theory, and modelling.

1 INTRODUCTION

The faulting mechanism in the Earth's crust is extremely multifaceted: some faults can be represented with a good approximation as planes, but in many cases this approximation is not sufficient as the fault surfaces may present bends and inflections and even bifurcations that generate complex geometries. A fault geometry is strictly connected with the peculiar geological setting of the area that surrounds it (Bürgmann & Dresen 2008; Copley 2017) and with the presence of fluids in the subsoil (Logan 1992). Ferrari & Bonafede (2012), use the asymptotic theory of generalized Cauchy kernel equations to study the singular behaviour of a strike-slip crack crossing the welded interface between two different media. They show that, in order to get a non-singular stress after faulting, the crack surface must change abruptly its dip across the interface or it may bifurcate to provide wedge shaped structures toward the surface. Unfortunately, a similar method cannot be easily extended to dip-slip cracks. The Anderson's theory (Anderson 1942) assumes that normal and reverse faults are generated, respectively, in extensive and compressive environments in which one of the principal stress axes is vertical. It also assumes that sliding occurs on optimally oriented fault planes where the modified Coulomb's fracture criterion

$$|\tau| = \begin{cases} -f_s\,(\sigma_n + p)\,, & \text{if } \sigma_n < 0 \\ 0, & \text{if } \sigma_n \geq 0 \end{cases} \tag{1}$$

(e.g. Jaeger & Cook 1976) is first fulfilled.

In eq. (1), τ and σ_n are, respectively, the shear and normal stresses acting on the fault plane ($\sigma_n < 0$ if compressive), f_s is the static friction coefficient of the fault plane, p is pore pressure and the cohesion term is neglected. The modified Coulomb's criterion provides the minimal condition that allows fault sliding and the Anderson's theory assumes that the optimal dip angle is the one for which sliding occurs with the lowest shear traction acting on the fault or, for a 2-D state of stress, with the maximum Coulomb stress $\sigma_c = |\tau| + f_s(\sigma_n + p)$ (e.g. Turcotte & Schubert 2002).

Most faults in the Earth's crust are in rough accordance with the Anderson's theory which predicts that normal and reverse faults have dip angles greater and smaller than 45°, respectively, as it is often observed (e.g. Jackson 1987; Copley 2017) even if a considerable number of faults have non-Andersonian geometries (e.g. Célérier 2008). Fractures near very shallow dipping faults can give rise to decollements (or detachments) generating large horizontal displacements of overlying rock sheets. These almost horizontal faults cannot be described by the Anderson's theory and a long debate has risen to explain the related mechanism (Voight 1976). Hubbert & Rubey (1959) proposed that in some conditions the pore pressure can be comparable to the lithostatic pressure (due for example to sediment compaction or dehydration reactions in metamorphism), thus allowing to fulfill the Coulomb's criterion even for very shallow dipping faults. However, this mechanism

does not work for low dipping normal faults because in this case the maximum principal stress is vertical and the pore pressure cannot be greater than the horizontal stress (Scholz 2002) in order to avoid hydrofracture.

Other examples of non-Andersonian fault geometries are listric faults (very common curved fault surfaces whose dip angle progressively decreases with depth generating an upward concave shape), low angle normal faults (Wernicke 1995, and reference therein) and high-angle reverse faults. The latter ones, as reviewed by Sibson (1990), could be explained as reactivation of pre-existing normal faults. At the same time in some cases low angle normal faults can be interpreted as the reactivation of pre-existing thrusts (Chiarabba & Amato 2003). Alternatively, Forsyth (1992) sustains that the formation of low angle normal faults is related to stress inhomogeneities that, within the lithosphere, could play an important tectonic role in accommodating extension. Heterogeneities (or anisotropy) of material properties could provide an easier pathway for extension than high-angle faulting. Following this suggestion, the present model aims to answer to the following questions: (i) Can non-Andersonian fault geometries be favoured by the presence of rigidity contrasts within the crust? and (ii) Is it possible to devise a method to predict the growth direction on the basis of elastic parameters? The present model is devoted to giving a quantitative answer to these questions.

In order to investigate the effect of rigidity contrasts on the geometry of dip-slip faults, we here present a 2-D crack model (plane strain) for quasi-static fault growth following the criterion of 'maximum energy release' or minimum final energy (e.g. Göldner & Sih 1977). The latter one is used in modelling the direction of crack surface extension (or propagation) as an alternative to the one perpendicular to the maximum tensile stress (e.g. Erdogan & Sih 1963; Gunnars *et al*. 1997). As in Selcuk *et al*. (1994), we assume the presence of a single interface where the elastic modulus of rigidity changes suddenly. Accordingly, the present model can be used to interpret locally complex geometries of faults in a heterogeneous crust.

Several models have been proposed to represent fault growth or to interpret fault geometry complexities either assuming that preferred directions are the ones maximizing the Coulomb stress (e.g. Olson & Cooke 2005; Pollard & Fletcher 2005), or optimizing the work budget even with support of experimental approaches (Yagupsky *et al*. 2014; McBeck et al., 2017, 2018). Some authors, instead, use strain energy density to predict preferred fault directions (e.g. Du & Aydin 1995; Okubo & Schultz 2005; Olson & Cooke 2005). Mohapatra & Johnson (1998) showed that the formation of listric faults on pre-existing thrust ramps can be energetically favoured by means of a finite element model based on the potential energy minimization approach (Melosh & William 1989), in agreement with the present model.

The fault growth, following energetic criteria, considers the creation of new fault surface without requiring the reactivation of pre-existing fault planes unlike models based on the Coulomb criterion (1). In particular the Anderson's theory assumes that pre-existing faults with all possible orientations are present before failure (Jaeger & Cook 1976), as the frictional shear strength $-f_s(\sigma_n + p)$ is a property of the surfaces (e.g. Scholz 2002) and a pre-existing fault plane is necessary in order to apply (1).

The present model is based on the boundary element method (BEM) and it allows us to represent crack growth through iterative addition of elements (e.g. Kame & Yamashita 1999; Gupta 2011) following a similar procedure to the one used by Maccaferri *et al*. (2010) when studying the propagation of dykes in proximity of an elastic discontinuity. We deploy a procedure representing a tectonic shear fault surface including the effect of residual frictional traction on the rupture surface after its formation. Friction is described as the product of a dynamic friction coefficient f_d times the effective normal stress, following the idea from Coulomb's time that on a pre-existing surface 'a static friction coefficient must be exceeded for slip to commence', while during sliding 'slip is resisted by a dynamic friction' (Scholz 2002). As in Kattenhorn & Pollard (1999), Kanamori & Heaton (2013) and McBeck *et al*. (2017) we consider a constant frictional resistance during sliding. Rate and state dependent friction laws account for a variable dynamic friction coefficient. We here neglect these effects on dynamic friction which account for a small percentage change per order of magnitude change in the slip rate (e.g. Scholz 2002). We will also show that our results are not affected by small variations of the dynamic friction coefficient.

1.1 Single dislocation model

The crack model to be solved consists in finding the Burger's vectors of dislocations given an assigned initial stress field S^0_{ij} and a residual stress assuming a plane strain configuration. The initial stress field is assumed lithostatic (Pollard & Fletcher 2005, p. 229), plus an additional tectonic loading acting along the x-axis

$$S^0_{zz} = -\rho g z;\ S^0_{xx} = -\rho g z + \Delta\sigma;\ S^0_{xz} = 0 \text{ (Initial stress field)}. \tag{2}$$

In eq. (2), ρ is the rock density and g is the gravity acceleration, while $\Delta\sigma$ represents the tectonic loading ($\Delta\sigma < 0$ represents a compressive tectonic loading), which gives rise to a shear component $\Delta\sigma_{\parallel}$ and a normal component $\Delta\sigma_{\perp}$ of traction acting on the fault surface. In the shallow low rigidity crust a laterally confined sedimentary basin can be considered with rigid vertical boundaries. In this case, as an alternative to a lithostatic stress field, a uniaxial initial strain state can be assumed. This alternative choice provides an initial horizontal component of the stress field $S^0_{xx} = -\frac{\nu}{1-\nu}\rho g z + \Delta\sigma$ where a tensile deviatoric stress of mechanical origin is present, which can favour the growth of a normal fault, despite a low tectonic stress $\Delta\sigma$ there. However, even in presence of sedimentation, the net horizontal deviatoric stress is expected to vanish after a typical geothermal gradient is restablished, due to the effect of related compressive thermal stresses (Turcotte & Schubert 2002), so we keep the assumption of eq. (2).

We can therefore compute the tectonic shear stress drop τ that must be released by the dislocation at its centre $(x_c,\ z_c)$ as $\tau = \tau^0 - \tau^1$. With τ^0 and τ^1 we indicate, respectively, the shear traction acting on the fault plane before and after the dislocation takes place. If we assume that the crack releases all the shear stress induced by the tectonic stress ($\tau^1 = 0$), we can express the stress drop as $\tau = \tau^0 = \Delta\sigma_{\parallel}$. Modelling

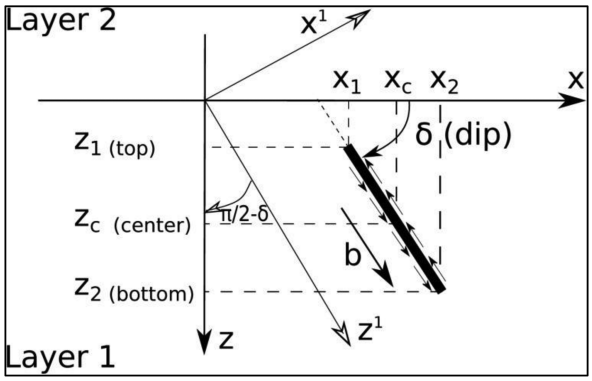

Figure 1. Scheme of variables and coordinates of a dislocation element. The top, centre and bottom coordinates are, respectively, (x_1, z_1), (x_c, z_c), (x_2, z_2). The dip angle is δ and the Burger's vector magnitude is indicated as b. We also represent the reference (x^1, z^1) system with z^1 parallel to the dislocation, that is obtained performed rotating the initial reference system (x, z) by an angle $\theta = \frac{\pi}{2} - \delta$.

fault friction requires the computation of the normal stress acting on the fault plane, $\sigma_n = -\rho g z + \Delta\sigma_\perp$ that corresponds to the normal stress induced by the lithostatic loading, plus the normal traction induced by the tectonic stress on the fault plane. In case of a 2-D dip-slip dislocation (Fig. 1) with a dip angle δ, $\Delta\sigma_\perp$ and $\Delta\sigma_\parallel$ can be written as:

$$\Delta\sigma_\parallel = -\frac{1}{2}\Delta\sigma \sin 2\delta \tag{3}$$

$$\Delta\sigma_\perp = \frac{1}{2}\Delta\sigma\,(1 - \cos 2\delta) \tag{4}$$

According to the Coulomb's criterion, fault slip occurs if

$$\left|-\frac{1}{2}\Delta\sigma \sin 2\delta\right| = f_s \left[\rho g z - p - \frac{1}{2}\Delta\sigma\,(1 - \cos 2\delta)\right]. \tag{5}$$

For a given dip-angle we can find the expression for the minimum magnitude of the tectonic stress that is able to generate slip as:

$$\Delta\sigma = \frac{2 f_s\,(\rho g z - p)}{f_s\,[1 - \cos 2\delta] \pm \sin 2\delta}\,. \tag{6}$$

The Anderson's theory assumes that fault slip occurs over a plane where $|\Delta\sigma|$ is minimum, whose angle can be found from the following equation, where the positive and negative determinations are, respectively, the solutions for reverse and normal faults.

$$\frac{\mathrm{d}\Delta\sigma}{\mathrm{d}\delta} = 0 \rightarrow \tan 2\delta = \pm\frac{1}{f_s} \quad \text{(Anderson's theory)}\,. \tag{7}$$

The energy release due to the dislocation in a homogeneous space can be written as (Scholz 2002)

$$\Delta E = \frac{1}{2}\int_\Sigma \left(\tau^0 + \tau^1\right) b\,\mathrm{d}\Sigma, \tag{8}$$

where Σ is the dislocation surface and b is the magnitude of the displacement discontinuity (Burger's vector). Since we are not considering opening components of the Burger's vector, b is the slip magnitude. It must be stressed that eq. (8) provides the energy difference between the static initial state (before any motion started) and the final static state (after any motion has damped out); in particular, eq. (8) expresses the total energy release, including the deformation (or elastic) energy and the gravitational potential energy (e.g. Kostrov 1974; Dahlen & Tromp 1998; Kanamori & Heaton 2013). The total energy release ΔE is spent to provide the fracture energy (necessary to create the fracture surface by breaking molecular bonds), to produce heat (through frictional processes related to surface slip) and to generate seismic waves.

In order to take into account the residual friction $\tau^1 = -f_d(\sigma_n + p)$, the shear stress drop must be redefined as in this case the dislocation does not release all the tectonic stress and $\tau = \tau^0 + f_d(\sigma_n + p)$ (Kattenhorn & Pollard 1999), where f_d is the dynamic friction coefficient. The magnitude of the Burger's vector or slip $b = |\mathbf{b}|$ is expressed in terms of the stress drop as

$$b = G_f\,\tau \quad \text{with} \quad G_f = \frac{\pi\,(\lambda + 2\mu)}{4\mu\,(\lambda + \mu)}\,W \tag{9}$$

(Stein & Wysession 2003), where W is the width of the fault in the dip direction while μ and λ are Lamè parameters and G_f is termed 'geometrical factor'. Then ΔE can be expressed as:

$$\begin{aligned}\Delta E &= \tfrac{G_f}{2}\int_\Sigma \left(\tau^{0^2} - \tau^{1^2}\right)\mathrm{d}\Sigma \\ &= \tfrac{G_f}{2}\int_\Sigma \left\{(\Delta\sigma \sin 2\delta)^2 - f_d^2\left[\rho g z - p - \tfrac{1}{2}\Delta\sigma(1 - \cos 2\delta)\right]^2\right\}\mathrm{d}\Sigma.\end{aligned} \tag{10}$$

In this section, we assume a hydrostatic pore pressure $p = \rho_f g z$, with $\rho_f < \rho$ density of the fluid (we shall also consider near lithostatic pore pressure later). The dislocation surface Σ can be rewritten per unit of length L along strike and in terms of the width W. In order to perform the integration, it is useful to express a width element in terms of depth z as $\Delta W = \Delta z / \sin\delta$ and then, following eq. 10 integrate along z from $z_1 = z_C - \frac{1}{2} W \sin\delta$ to $z_2 = z_C + \frac{1}{2} W \sin\delta$ (Fig. 1), where z_C is the dislocation centre

$$\begin{aligned}\Delta E = & \frac{G_f L}{2} \int_{z_1}^{z_2} \left\{ \left[-\frac{1}{2}\Delta\sigma \sin(2\delta) \right]^2 - f_d^2 \right. \\ & \left. \left[(\rho - \rho_f) g z - \frac{1}{2}\Delta\sigma (1 - \cos(2\delta)) \right]^2 \right\} \cdot \frac{1}{\sin(\delta)} \, \mathrm{d}z \\ = & \frac{G_f L}{2} \left[\Delta\sigma^2 \sin^2\delta \cos^2\delta \, W - \frac{f_d^2 (\rho - \rho_f)^2 g^2 W^3}{12} \right. \\ & \left. \sin^2\delta - f_d^2 (\rho - \rho_f)^2 g^2 z_c^2 W - f_d^2 \Delta\sigma^2 W \sin^4\delta + 2(\rho - \rho_f) g W \Delta\sigma f_d^2 z_C \sin^2\delta \right]. \end{aligned} \tag{11}$$

It is worth to notice that the condition $\Delta E = 0$, leads to the Anderson's prediction with f_d replacing f_s (eq. 6). This sounds reasonable because the Coulomb criterion used in the Anderson theory provides a condition for sliding on a pre-existing surface to start, while a finite energy release is accomplished only during the development of a finite sliding (b in eq. 8). Now we can find the dip angle δ that maximizes the energy release by imposing $\frac{\mathrm{d}\Delta E}{\mathrm{d}\delta} = 0$ from which we obtain (eq. 12):

$$\sin^2\delta = \frac{f_d^2 (\rho - \rho_f)^2 g^2 W^2 - 24(\rho - \rho_f) g \Delta\sigma f_d^2 z_C - 12\Delta\sigma^2}{-24\Delta\sigma^2 (1 + f_d^2)} . \tag{12}$$

In order to allow the fault surface growth and consequently the fault sliding, according to the energetic criterion, we assume that the energy release per unit length must be greater than the sum of the work E_f done against friction and the fracture energy $E_T(W)$ (per unit length), requested to create a fault surface $L \times W$, that is $\Delta E > E_f + E_T$. In particular:

1. E_f which is released from the fault as thermal energy (e.g. Mulargia *et al*. 2004) is given by

$$E_f(W) = -f_d (\sigma_n + p) W b \tag{13}$$

Since the friction work cannot be negative, then in eq. (13) $E_f = 0$ for $\sigma_n + p > 0$.

1. E_T depends on the Poisson's modulus ν and on the specific surface fracture energy γ_s that is $E_T(W) = 2(1 - \nu^2)\gamma_s W$ (Griffith 1921) with $\gamma_s \approx 1$–$10\ \mathrm{J\,m^{-2}}$ for most materials, but for some earthquakes it can reach much higher values, up to $10^6\ \mathrm{J\,m^{-2}}$ (Scholz 2002; Thio 2009, p. 30).

In Figs 2(a) and (b) we plot the energy release and the energy dissipated against friction per unit of length obtained for different dip angles, respectively for a reverse ($\Delta\sigma < 0$) and a normal ($\Delta\sigma > 0$) fault. Imposing the same magnitude of tectonic stress $|\Delta\sigma|$ and using the same dynamic friction coefficient $f_d = 0.3$, a normal fault produces a much greater energy release ΔE with respect to a reverse fault. In fact, in the case of a normal fault, the extensive tectonic stress leads to a lower τ[1] (i.e. to a greater stress drop τ). Due to the lower $|\sigma_n|$, an extensive tectonic environment also produces a lower dissipation of the friction energy E_f with respect to a compressive tectonic environment. In case of a normal fault with high dip angle, the tectonic stress can be so high to make σ_n positive at shallow depth leading to the vanishing of the friction effects even for angles close to those maximizing ΔE (Fig. 2b). In Figs 2(c) and (d), we plot ΔE computed with different tectonic loading magnitudes $|\Delta\sigma|$, respectively, for a reverse and normal fault. Curves with ΔE always negative indicate that the tectonic stress is not able to allow the sliding of the fault regardless of its dip angle. A comparison between the Anderson's criterion and the energy criterion can be made by considering $f_s = f_d$. We recall that, the direction of the crack growth, according to the energetic criterion, depends on the total tectonic stress acting on the fault plane which may be greater than the minimum tectonic stress capable of generating slip according to the Anderson's theory. In this case, it is worth to note that for both reverse and normal faults, as the energy release increases, its maximum is reached for dip angles that deviate most from the Anderson's solution. This means that the maximum energy release criterion provides, respectively, greater and smaller dip angles for reverse and normal faults with respect to the Anderson's condition (eq. 7), while we recall that the same solution is obtained only if $\Delta E \to 0$ with f_d replacing f_s. It is worth to notice that the difference between ΔE and E_f for both normal and reverse faults decreases with a lowering of ΔE (Figs 2a and b) and if $\Delta E \to 0$ then $E_f > \Delta E$; this means that the dip angle provided by the Anderson's criterion is energetically unable to produce fault sliding.

2 MODEL

2.1 The stress computation

In order to model the crack growth, we firstly need to set up a suitable representation of the stress field generated by a 2-D fault, arbitrarily placed in a medium consisting of two welded half-spaces, each of which with assigned elastic parameters (layer $l = 1$, in $z > 0$, is assumed to

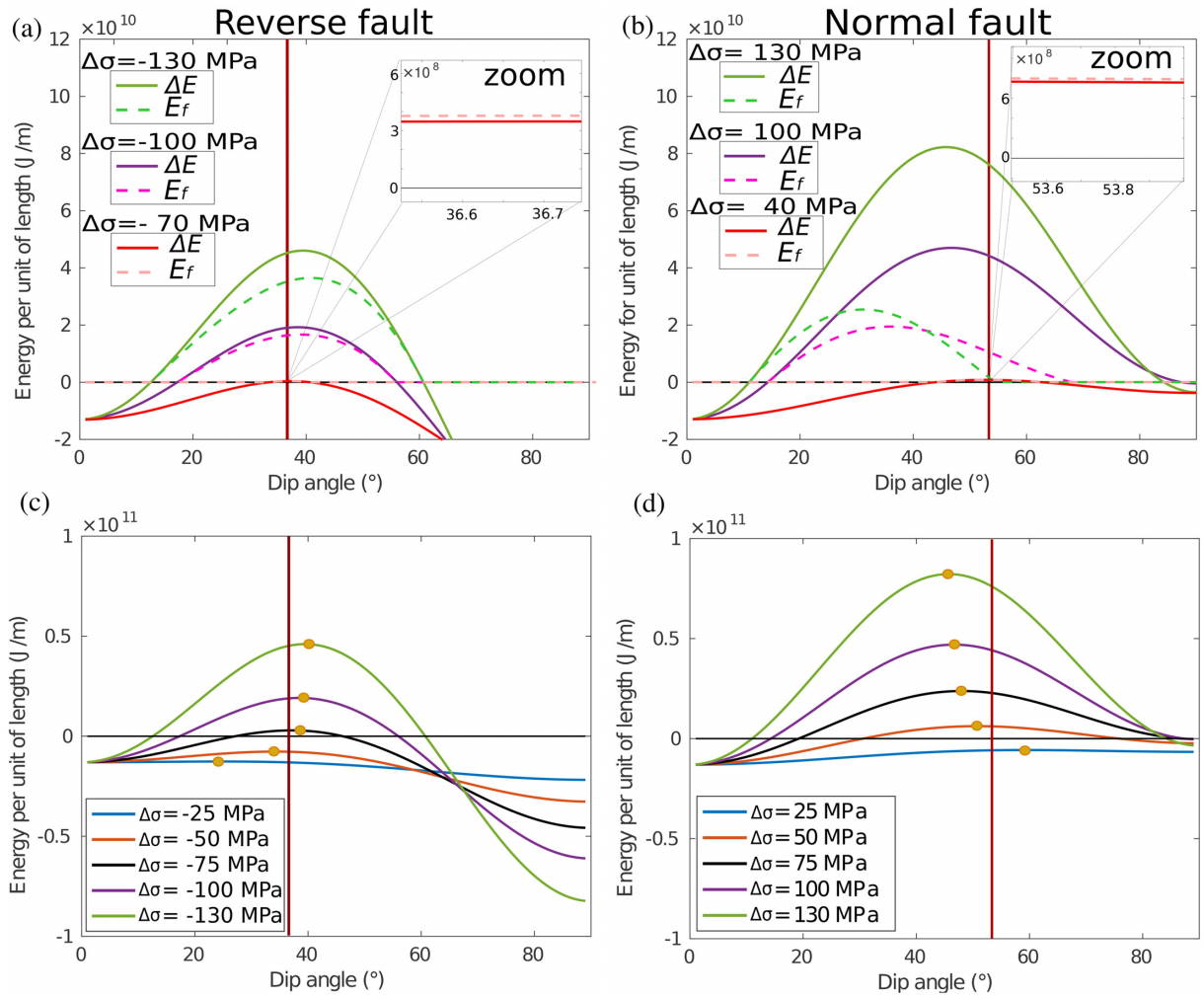

Figure 2. Energy release (solid lines) per unit length, ΔE, as a function of the dip angle in case of reverse (a) and normal faults (b). The two cases shown have $|\Delta\sigma| = 100$ and 130 MPa and $f_d = 0.3$. The dashed lines are frictionally dissipated energy per unit length, E_f, as functions of the dip angle. In bottom panels $\Delta E(\delta)$ is plotted for different $|\Delta\sigma|$ ranging from 25 to 130 MPa. Yellow dots indicate the maximum of the curves for both reverse (c) and normal (d) faults. The vertical red lines represent the Anderson's solution for the dip angle computed with a $f_s = 0.3$. A fault width $W = 1$ km and $z_c = 5$ km are assumed, for each fault mechanism. The rock and pore fluid densities are 2800 and 1000 kg m^{-3}, respectively.

lay below layer $l = 2$, in $z < 0$). As we represent fault elements as closed Volterra dislocations (with uniform b), we firstly need to compute the stress field generated in the two half-spaces by elementary dislocations. For this purpose, we use analytic solutions for semi-infinite vertically dipping edge and tensile dislocations in a layered medium provided by Rivalta *et al*. (2002) and Bonafede & Rivalta (1999). They distinguish two different cases: in the first one the dislocation surface is entirely embedded in one half-space and in the second one the dislocation crosses the elastic discontinuity interface. This approach is functional to our scope since in order to represent the crack growth we must be able to model a fault that is initially embedded in one half-space, but during its growth it may cross the elastic discontinuity surface.

We firstly introduce the stress tensors s_{ij}^T due to a semi-infinite, vertically dipping tensile (apex 'T', equations (31, 32, 35 and 37) in Bonafede & Rivalta 1999). We also introduce s_{ij}^E for a vertical edge dislocation surface (apex 'E', equations (27, 28, 31 and 33) in Rivalta *et al.* 2002). Both kinds of dislocation $\{x = 0,\ z > z_1\}$ have unitary Burger's vector. In the following equations the stress tensor s_{ij} for both kinds of dislocation is computed in each layer l as the difference between the stress tensor solution in a homogeneous unbounded medium (h_{ij}^l) with the same elastic properties of layer 'l' and the Galerkin component (g_{ij}^l) computed in the half-space 'l', that is necessary to provide the continuity of displacements and tractions across a welded interface. In our notation indexes 'i' and 'j' represent the 2-D coordinates (x, z).

$$s_{ij}^T(x,z;z_1) = \begin{cases} h_{ij}^{T,1}(x,z;z_1) - g_{ij}^{T,1}(x,z;z_1), & z > 0 \\ h_{ij}^{T,2}(x,z;z_1) - g_{ij}^{T,2}(x,z;z_1), & z < 0 \end{cases} \tag{14}$$

$$s_{ij}^E(x,z;z_1) = \begin{cases} h_{ij}^{E,1}(x,z;z_1) - g_{ij}^{E,1}(x,z;z_1), & z > 0 \\ h_{ij}^{E,2}(x,z;z_1) - g_{ij}^{E,2}(x,z;z_1), & z < 0. \end{cases} \tag{15}$$

For a generic semi-infinite inclined dip-slip dislocation with top placed in $x = x_1 \neq 0$ and dip angle δ, we need to translate eqs (14) and (15) by $x \rightarrow x - x_1$ (Fig. 1) and to combine them as follows (e.g. Maccaferri *et al.* 2010) in order to obtain a dip-slip dislocation with dip angle δ and unit Burger's vector:

$$s_{ij}\ (x, z; x_1,\ z_1,\ \delta) = \ -\cos\delta s^T_{ij}\,(x, z; x_1, z_1) + \sin\delta s^E_{ij}\,(x, z; x_1, z_1)\,. \tag{16}$$

In order to find the stress field $s^{(\text{closed})}_{ij}$ due to a unitary Burger's vector for a closed dip-slip dislocation with its center point in (x_c, z_c) (Fig. 1), we need to subtract from eq. (16) the solution of a semi-infinite dislocation with top in (x_2, z_2) having the same dip angle δ:

$$s^{(\text{closed})}_{ij}\,(x, z; x_c,\ z_c,\ \delta) = s_{ij}\,(x, z; x_1,\ z_1,\ \delta) - s_{ij}\,(x, z; x_2, z_2, \delta)\,. \tag{17}$$

From eq. (17) and performing a rotation of the reference frame by $\theta = \frac{\pi}{2} - \delta$, which brings (x, z) into (x^1, z^1) as sketched in Fig. 1, we can then compute the shear ($I = s^{(\text{closed})}_{x^1 z^1}$) and the normal ($Y = s^{(\text{closed})}_{x^1 x^1}$) tractions acting on an oriented dislocation plane with dip angle δ. Finally, we obtain the stress field σ_{ij} generated by the closed dip-slip dislocation by multiplying $s^{(\text{closed})}_{ij}$ by b, that is defined from here on out as $b = \pm|\mathbf{b}|$, where $\mathbf{b}$ is the Burger's vector or slip

$$\sigma_{ij}\,(x, z; x_c,\ z_c,\ \delta) = b \cdot s^{(\text{closed})}_{ij}\,(x, z; x_c,\ z_c,\ \delta)\,. \tag{18}$$

It is worth to notice that according to our notation, if $0° \leq \delta \leq 90°$, b is positive for a reverse fault and negative for a normal fault. As an example, Fig. 3 shows the resulting shear and normal stress components and the Coulomb failure function (CFF) for a dip-slip dislocation with $\delta = 30°$, $f_s = 0.4$ and $b = 1$ m embedded in a medium containing an elastic discontinuity. In the half-space where the dislocation takes place, the stress components have similar pattern as those obtained in a homogeneous half-space (Figs 3a, b and c), with the exception of the areas closest to the material discontinuity. If the rigidity in the upper half-space (which does not contain the dislocation) is lower, the stress components have a much lower intensity, due to the step-like decrease of the rigidity modulus (Figs 3d, e and f). Otherwise if the rigidity of the upper half-space is greater, there stress lobes are wider with respect to the ones in the lower half-space, due to the step-like increase of the rigidity modulus (Figs 3g, h and i).

2.2 The boundary element model

Once we know the shear stress I and the normal stress Y provided by a unitary slip, we can find the magnitude of the Burger's vector required by the crack to generate an assigned shear stress drop by imposing $bI = -\tau$, where τ is the shear stress drop on the fault plane.

According to the boundary element technique, we model a fault as a crack split up into N interacting closed dislocation elements. Then we can find the slip on each elementary dislocation ($b = b_k$, $k = 1,\ldots, N$) imposing that equilibrium of stresses holds at the mid-point of the dislocation element (Maccaferri *et al.* 2010). In absence of friction this means that we have to solve the following $N \times N$ linear system.

$$\begin{cases} \sum_{k=1}^{N} b_k\ I_{1k} = -\tau_1^0 \\ \qquad\cdots \\ \qquad\cdots \\ \sum_{k=1}^{N} b_k\ I_{Nk} = \ -\tau_N^0 \end{cases}. \tag{19}$$

In system (19) the terms τ_m^0 ($m = 1,\ldots, N$) represent the shear tractions of tectonic origin released at the midpoint of the mth dislocation element, while I_{mk} are called 'influence coefficients'. They represent the shear stresses computed at the midpoint of the mth dislocation due to the kth dislocation with unitary Burger's vector, also accounting for self shear-stress generated by each dislocation element on its surface (when $m = k$). It is worth to notice that, differently from Maccaferri *et al.* (2010) who represent a dike as a crack with a $2N$ x $2N$ linear system, we do not need to impose the equilibrium of normal stresses of the crack since we are assuming that the Burger's vectors (i) have no normal component and (ii) in absence of friction the environmental normal stress $\sigma_n + p$ has no influence on fault equilibrium; hence the problem to be solved is a system of N equations with N unknowns (system 19).

2.2.1 Including the fault friction

If we consider as final traction on the fault the dynamic frictional resistance, the shear stress of tectonic origin is not completely released as it is in (19) and for a crack represented by N different dislocation elements, we have to generalize the equilibrium sets of equation as follows:

$$\begin{cases} \sum_{k=1}^{N} b_k\,(I_{1k} + f_d Y_{1k}) = \ -\left[\tau_1^0 + f_d(\sigma_{n1} + p_1)\right] \\ \qquad\qquad\cdots \\ \qquad\qquad\cdots \\ \sum_{k=1}^{N} b_k\ (I_{Nk} + f_d Y_{Nk}) = \ -\left[\tau_N^0 + f_d(\sigma_{nN} + p_N)\right] \end{cases}, \tag{20}$$

where σ_{nm}, p_m $m = 1,..N$ are the environmental normal stress components and pore pressure on the m-*th* dislocation. Compared to the Rivalta *et al.* (2002) paper, here the z-axis origin is translated in order to have the elastic discontinuity at a vertical coordinate $z_0 > 0$ where the lithostatic pressure (evaluated starting from $z = 0$) has values pertinent to typical seismogenic depths (a few km). In (20) the frictional

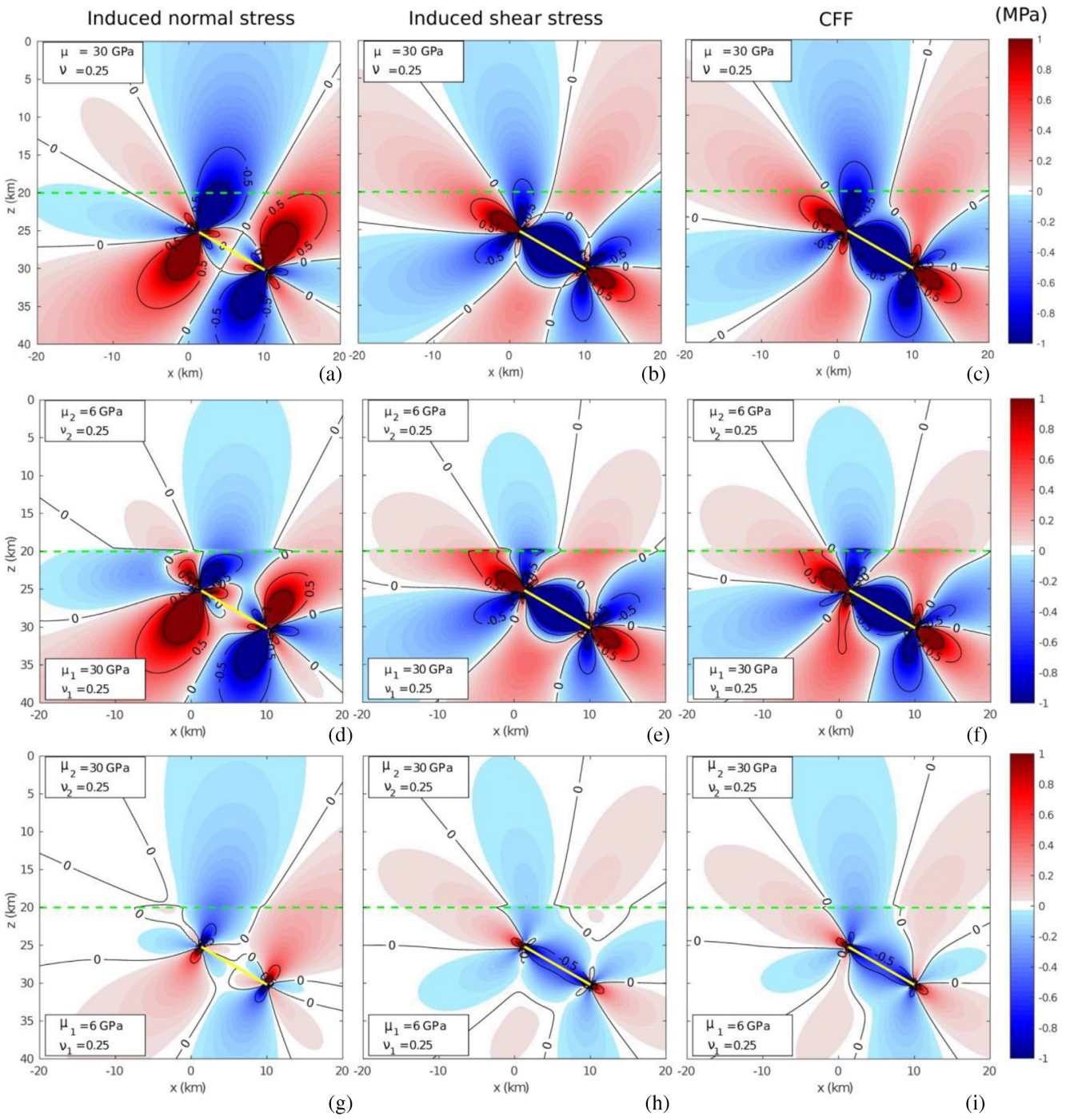

Figure 3. Induced normal (a, d, g) and shear (b, e, h) stress and Coulomb failure function (c, f, i), CFF = shear stress + fsnormal stress generated by a reverse dislocation (yellow segment) with b = 1 m, $f_s = 0.4$ and $\delta = 30^\circ$ in a layered medium. The green dashed line represents the elastic discontinuity. CFF is computed considering a receiving fault with the same dip as the dislocation source. The homogeneous medium (a, b and c) has a rigidity $\mu = 30$ GPa and a Poisson's modulus $\nu = 0.25$. Indicating with μ_1 the rigidity of the deeper layer and μ_2 the rigidy of the shallower one, in panels d, e and f $\mu_1 = 30$ GPa and $\mu_2 = 6$ GPa, while in panels g, h and i $\mu_1 = 6$ GPa and $\mu_2 = 30$ GPa. The Poisson ratio is $\nu = 0.25$ everywhere. Colour and contour represent stresses magnitude expressed in MPa.

terms (those multiplied by f_d) are kept only if they are positive. The influence coefficients Y_{mk}, represent the normal stresses computed at the midpoint of the mth dislocation element due to the kth dislocation element with unitary Burger's vector and they are needed to include the normal stresses generated by the interaction among the N elements that make up the crack. It is worth to notice that in a homogeneous medium $Y_{mk} = 0$ when $m = k$ since faults do not generate self-induced normal stress (Fig. 3a). This is no longer true in the case of a layered medium, as the feedback interaction with the discontinuity leads to an induced normal stress that is not simply antisymmetric with respect to the fault plane (Figs 3d and g). Of course, in absence of friction ($f_d = 0$) the system (20) reproduces system (19).

2.3 The crack growth

Our model of fault growth represents a quasi-static crack propagation, that is a slower increase of the slip surface than during the dynamic rupture propagation. While the latter characterizes the coseismic stage of the fault cycle, here we assume that the fault surface can extend both through seismic and aseismic slip (Gudmundsson *et al*. 2013) during subsequent earthquakes whose slip surface is adjacent and almost coplanar with the one created by the last event occurred, as for example during main shock–aftershock sequences (e.g. Convertito *et al*. 2013) or during swarms (Hainzl & Fischer 2002). Fault growth is often observed laterally, that is close to the along-strike direction, as, for example during subsequent earthquakes occurring along a plate boundary or a tectonic lineament (e.g. Nalbant *et al*. 2005; Tallarico *et al*. 2005). However, from observation near the surface even the upwards fault growth is envisaged (e.g Baudon & Cartwright 2008). Accordingly, in our model, during the quasi-static fault growth, the configuration at a given instant of time is interpreted as the cumulative effect of successive dislocation events (Cowie & Scholz 1992) fulfilling the crack requirement (19) or (20) and occurring on adjacent fault patches.

We start from an initial crack constituted by N dislocation elements with the same width $\Delta W = d$ (i.e. the total width is $W = Nd$) and the same dip, in order to simulate a planar fault surface. From this configuration we apply the boundary element criterion in order to find the Burger's vector of each dislocation element and then we can estimate the strain energy accounting for a friction dependent stress drop (Cooke & Murphy 2004) which reduces the amount of energy per unit length available for crack growth to:

$$\Delta E\,(W) = \sum_{m=1}^{N} \frac{d}{2}\,\{b_m \cdot [\tau_m - f_d\,(\sigma_{nm} + p_m)]\} \tag{21}$$

We can also describe the work done against friction (per unit length), which is dissipated as thermal energy, as:

$$E_f\,(W) = -\sum_{m\,=\,1}^{N} d \cdot b_m \cdot f_d\,(\sigma_{nm} + p_m) \quad \text{where} \quad E_{fm} = 0 \;\; if\;\; \sigma_{nm} + p_m \geq 0 \tag{22}$$

The crack growth is simulated by adding a dislocation element beyond the tip of the crack and recomputing the new equilibrium using the boundary element technique with $N + 1$ dislocation elements. According to the theoretical formulation, the crack growth at each iteration is allowed if $b_k > 0,\ k = 1,\ N + 1$ and the energy release is greater than the fracture energy and the friction dissipated energy $\Delta E(W + d) > E_f(W + d) + E_T(W + d)$ (we use $\gamma_S = 1\ \mathrm{J\,m^{-2}}$). In order to model a variable direction of crack growth, the dip angle of the additional dislocation element (δ_{N+1}) is the one that maximizes the energy release (eq. 8) and it is chosen exploring different configurations with one degree dip-angle variations with respect to the dip, δ_N, of the adjacent dislocation element ($\delta_{N+1} \in [\delta_N\text{-}6^\circ, \delta_N + 6^\circ]$). The scheme of the crack growth procedure is shown in Fig. 4. According to Hirano & Yamashita (2015) and Kusakabe & Kame (2017), during the dynamic crack propagation on prescribed surfaces, large changes of the energy release rate may occur with respect to the monotonic increase expected in a homogeneous medium only when the fault tip gets very close to the elastic interface and is affected by reflected waves. Thus, the present quasi-static model likely overestimates the interface effects if applied to the dynamic crack propagation.

2.4 Study cases

We perform four different sets (SET) of simulations (SIM). In SET1 we preliminarily model different crack growths starting from planar faults with different dip-angles in a homogeneous medium with no friction. In the following set of simulations, we consider starting faults with a dip-angle of 30° for reverse fault and 45° for normal faults, as we will see that this starting parameter is not crucial. In SET2-4 we perform several simulations considering two welded half-spaces with rigidity ratios $r = \mu_1/\mu_2$, where the half-space 1 is the deepest one. In SET2 we consider uniform tectonic loading $\Delta\sigma$ and vanishing friction. In SET3 and SET4 we assume a rigidity-scaled tectonic loading, so that in the low rigidity layer we assume $\Delta\sigma_{\mathrm{low}} = \Delta\sigma\,\mu_{\mathrm{low}}/\mu_{\mathrm{high}}$. This condition reflects the case in which the tectonic stress is lower in the low rigidity layer and higher in the stiffer layer, in order to provide a vertically uniform strain. While in SET3 we consider no friction, in SET4 we investigate the effect of the dynamic friction coefficient on the crack growth in a tectonic environment and we focus on the difference between normal and reverse faults. For SET4 we use a hydrostatic pore pressure profile as a function of depth: $p\,(z) = p_f(z) = \rho_f\,gz$. To consider the case of high pore pressure we also assume $p(z) = p_{lit}(z) = \rho gz$ for compressive environments, while, in order to avoid hydro-fracture, $p\,(z) = \rho gz - \Delta\sigma$ for extensive environments ($\Delta\sigma > 0$) is used. The simulations parameters are reported in Table 1. The initial planar fault is constituted by 10 dislocation elements with a length of 100 m each. For SET4 we assign a value to the tectonic stress and rigidity of the stiffer layer ($\Delta\sigma = 60$ MPa for normal faults, $\Delta\sigma =$ -150 MPa for reverse faults and $\mu = 30$ GPa), while tectonic stress and rigidity of the less rigid layer are computed, respectively, according to the rigidity ratio 'r' ($\mu_{\mathrm{lower}} = \mu r$ if $r < 1$, $\mu_{\mathrm{lower}} = \mu/r$ if $r > 1$). The magnitude of $|\Delta\sigma|$ is chosen as it is a reasonable value for both normal and reverse faults (Copley 2017). The lithostatic pressure is computed assuming a constant rock density along depth $\rho = 2800\ \mathrm{kg\,m^{-3}}$. In all the simulations a maximum number of 50 iterations was imposed (i.e. the maximum number of dislocation elements is 60).

3 MODELLING RESULTS

Fig. 5 shows the SET1 resulting crack growth in a homogeneous medium without friction. Apart from the academic interest in separating effects due to the different parameters affecting crack growth, this case may apply to fault surfaces with negligible residual stress which are usually expected in near-lithostatic pore pressure environments (Hubbert & Rubey 1959), even if this assumption is not exactly equivalent to

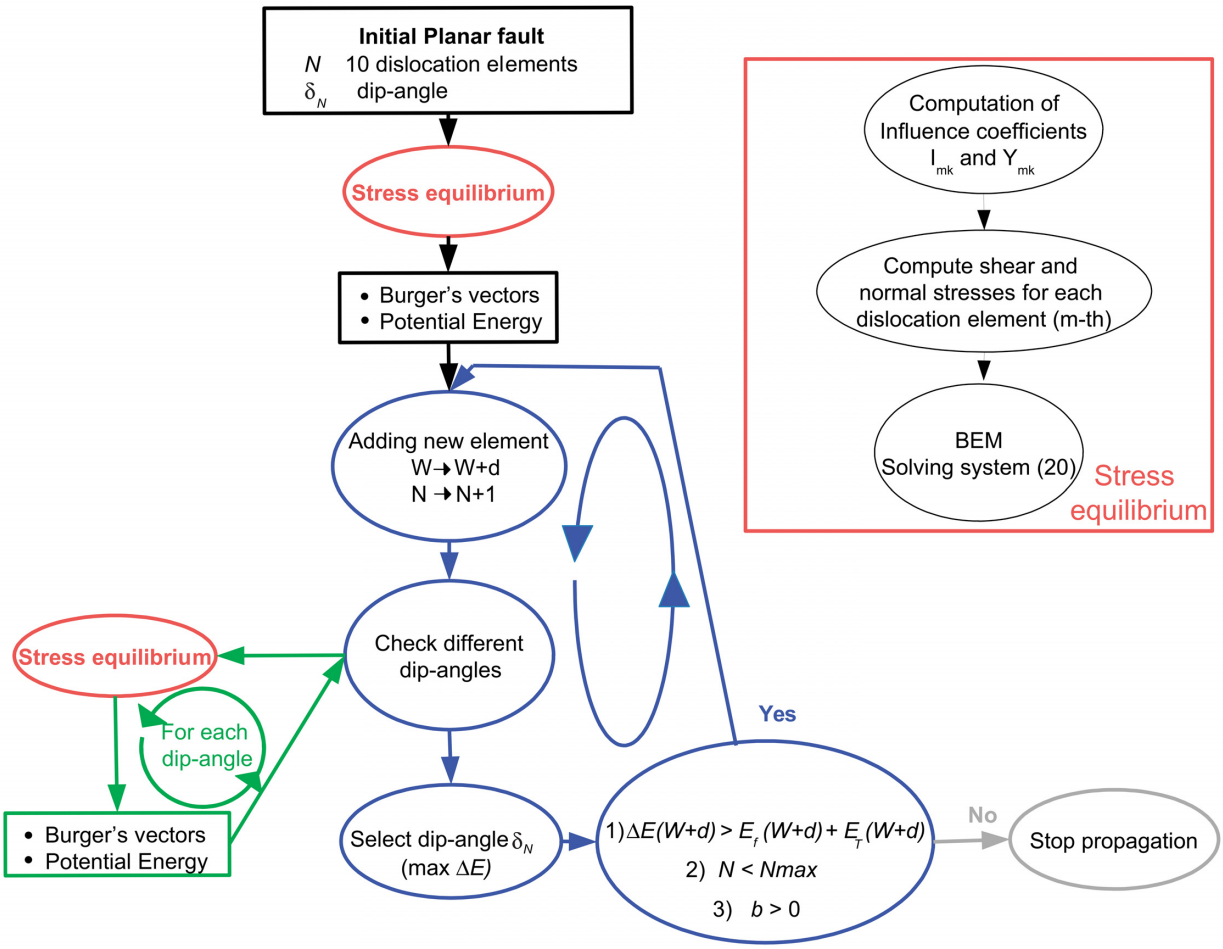

Figure 4. Iterative scheme of the crack growth modelling. During the growth the 'Stress equilibrium' function is recalled several times.

the one of a vanishing friction coefficient, as will be seen in the following of this section. In all cases of SET1, the crack growth following the energetic criterion tends to rapidly bend to the dip of about 45°, which corresponds to the direction of the maximum shear stress and therefore to the maximum energy release (eq. 12 with $f_d = 0$). The small deviation from 45° obtained in SIM1, 2 and 4 are due to the fact that the dislocation segments above the top of the starting fault are affected by the mechanical interaction with the dislocation elements of the initial fault plane. If the dip angle of the starting fault is lower than 45° (SIM1 and SIM2) the crack propagates with an angle slightly bigger than 45°, the opposite happens for dip angles of the initial fault greater than 45°. In any case we argue that the dip angle of the initial fault plane has little influence on the direction of crack growth and, in the subsequent sets of simulations, we keep fixed the starting dip-angle, in order to focus on the influence of the other parameters of the model.

Fig. 6(a) shows the results of SET2 simulations where the crack growth occurs without friction in a layered medium with rigidity ratio 'r' and the tectonic stress is assumed constant along depth. According to the equations of the previous sections, the crack growth depends on the tectonic stress profile $\Delta\sigma(z)$. The assumption of a vertically uniform tectonic stress is suitable to represent the brittle, shallow crust in the first 5 km (McGarr & Gay 1978; Kattenhorn & Pollard 1999). For comparison, we also report the result of SIM3 obtained in the homogeneous medium ($r = 1$). In all simulations of SET2 cracks quickly bend towards the same direction of 45° as in SET1 up to 1 km from the discontinuity, then the growth direction changes significantly depending on the magnitude of the rigidity contrast. If $r < 1$ (the crack approaches a higher rigidity layer) the dip angle has a rapid decrease that is greater for smaller r. For $r = 0.05$ (SIM5) the crack follows the elastic discontinuity line (dip goes to 0). If $r > 1$, (the crack propagates towards a lower rigidity layer), the dip angle has a rapid increase, but it decreases again while rising upwards. For all simulations of SET2 except for the limit case of SIM5, the crack, while moving away from the discontinuity and rising, tends to bend asymptotically towards the 45° dip following the direction of maximum shear stress, as expected in a homogeneous space.

Fig. 6(b) shows the results of SET3 that has the same parameters of SET2 but the tectonic stresses are scaled with the rigidity modulus of the two layers. This assumption leads to a constant tectonically induced strain along the model boundaries and demand that the two layers of the crust must remain welded (Kusznir & Park 1984; Bürgmann & Dresen 2008). In these cases, the main results of Fig. 6(a) are confirmed, as the rigidity contrast induces a curvature on the crack growth: if $r > 1$ ($r < 1$) the dip-angle of the crack increases (decreases) near the discontinuity. Unlike the SET2 simulations, however, in SET3 the resulting cracks with $r < 1$ bend more quickly to 45° after passing the

Table 1. Parameters of simulations concerning a crack growth starting in layer 1 (below) and propagating towards layer 2 (above) with different rigidity moduli μ_1 and μ_2. Rows report in order: simulation number, rigidity ratio $r = \mu_1/\mu_2$, starting dip angle δ, dynamic friction coefficients in layer 1 (f_{d1}) and 2 (f_{d2}), notes on crack growth stopping. The rigidity and the tectonic stress in the stiffest layer are $\mu = 30$ GPa and $|\Delta\sigma| = 0.1$GPa (SET 1 to 3), respectively. In SET3 and 4 the tectonic stress $\Delta\sigma_{\text{low}}$ of the less rigid layer (with rigidity μ_{low}) is computed according to $\Delta\sigma_{\text{low}} = \Delta\sigma\,\mu_{\text{low}}/\mu$. The initial planar fault is constituted by 10 dislocation elements with a length of 100 m each. In SET4 different pore pressure vertical profiles are considered ($p = p_f$, p_{lit}, $p_{lit} - \Delta\sigma$) and the tectonic stress is $\Delta\sigma = 0.06$ GPa for normal faults and $\Delta\sigma = -0.15$ GPa for reverse faults, except for the simulation 22 N in which $\Delta\sigma = 0.03$ GPa. The density of pore fluids and crust is assumed as 1000 and 2800 kg m^{-3}, respectively.

	SIM	$r = \mu_1/\mu_2$	Starting δ	f_{d1}	f_{d2}	$\Delta\sigma$	Growth stop	
SET1	1	1	0	0	0	Constant		No
	2	1	30°	0	0	Constant		No
	3	1	45°	0	0	Constant		No
	4	1	90°	0	0	Constant		No
SET2	5	0.05	30°	0	0	Constant		No
	6	20	30°	0	0	Constant		No
	7	5	30°	0	0	Constant		No
	8	0.2	30°	0	0	Constant		No
SET3	9	0.05	30°	0	0	Scaled		No
	10	20	30°	0	0	Scaled		Yes
	11	5	30°	0	0	Scaled		No
	12	0.2	30°	0	0	Scaled		No
	13	1	30°	0	0	Scaled		No
SET4							$p = p_f$	$p = \begin{cases} p_{lit} & (R) \\ p_{lit} - \Delta\sigma & (N) \end{cases}$
	14R and 14N	5	30°(R)/45° (N)	0.3	0.3	Scaled	Yes	Yes
	15R and 15N	0.2	30°(R)/45° (N)	0.3	0.3	Scaled	It does not start	No
	16R and 16N	0.2	30°(R)/45° (N)	0.05	0.3	Scaled	No	No
	17R and 17N	1	30°(R)/45° (N)	0.3	0.3	Scaled	No	No
	18R and 18N	2	30°(R)/45° (N)	0.3	0.3	Scaled	No	No
	19R and 19N	0.05	30°(R)/45° (N)	0.3	0.3	Scaled	It does not start	Yes (R), No (N)
	20R and 20N	0.05	30°(R)/45° (N)	0.05	0.3	Scaled	It does not start	No (R), No (N)
	21R and 21N	1	30°(R)/45° (N)	0.05	0.3	Scaled	No	No
	22N	4	10°dip, long detachment	0.3	0.3	Scaled	$p = p_f$	
			Detachment friction	$f_d = 0.05$			No	

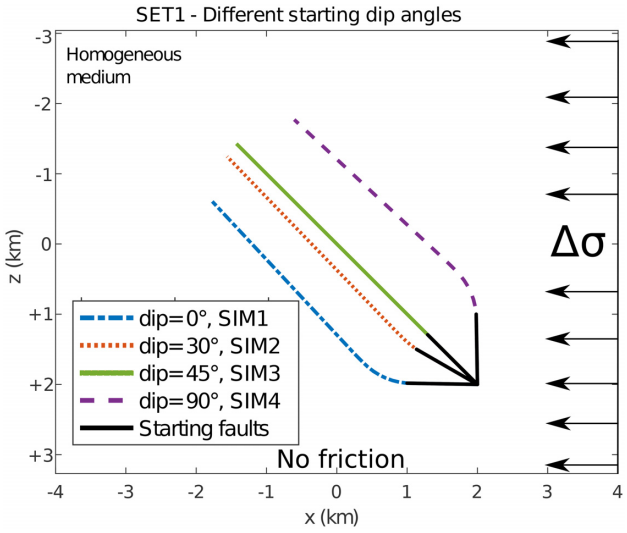

Figure 5. Crack growth pattern (coloured lines) obtained in simulations of SET1 (homogeneous elastic medium, absence of friction), for a starting planar fault (black lines) with different dip angles: SIM1 ($\delta = 0°$), SIM 2 ($\delta = 30°$), SIM 3 ($\delta = 45°$) and SIM 4 ($\delta = 90°$). The tectonic stress $\Delta\sigma = 100$ MPa is assumed uniform along depth.

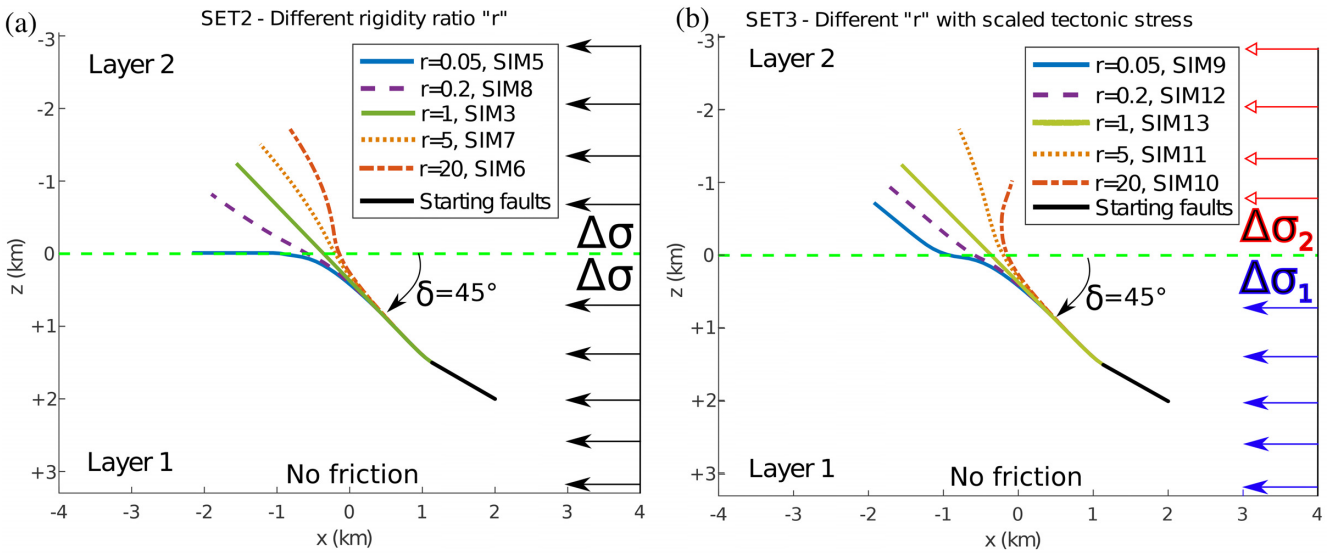

Figure 6. Crack growth pattern (coloured lines) obtained in simulations of SET2 and SET3 (heterogeneous elastic medium, absence of friction). The tectonic stress $\Delta\sigma = 100$ MPa is assumed uniform over depth in SET2 (a) while in SET3 (b) it is rescaled according to the rigidity ratio r. The simulations have different rigidity ratios. Starting planar faults (black lines) have a dip-angle $\delta = 30^\circ$. The green dashed line shows the elastic discontinuity. The dip angle attained by the crack before meeting the discontinuity is indicated.

discontinuity. In the case of SIM9 the crack follows the layer interface for about 1 km, but unlike SIM5, after a few iterations, it finds enough energy to cross it. In cases with $r > 1$, the dip increase is much more pronounced compared to the SET2 simulations due to the fact that the interaction among the fault segments is more important because the upper, less rigid layer has a lower tectonic stress. SIM11 gives rise to a two-segment fault with different dip-angles, while SIM10 reaches a dip angle $\delta > 90^\circ$ and it is the only simulation of SET1 that stops growing. It is worth to notice that results of SET1 to SET3 are the same for both normal and reverse environments as they only depend on the shear stress modules (eqs 19 and 21), which are the same for both fault mechanisms. This is no longer true in presence of friction (SET4) as the normal stress generated by a reverse dislocation (Figs 3a, d and g) has an opposite sign with respect to that of a normal dislocation, so in SET4 we distinguish the results of simulations of normal and reverse faults, indicated, respectively with "*N*" and "*R*" in Table 1 (Figs 7 and S1).

Figs 7(a) and (b) show the results of reverse faults obtained including the dynamic friction coefficient, $f_d = 0.3$, that is assumed constant along depth. The main effect of friction is that the crack growth, far from the elastic discontinuity, proceeds with a dip-angle not greater than 40° regardless of the p profile, differently from what occurs in absence of friction. For instance, in absence of friction, $r > 1$ leads to crack dip >45° near the discontinuity (Fig. 6).

Figs 7(c) and (d) show the results of SET4 simulations for an extensional tectonic environment ($\Delta\sigma > 0$) that gives rise to the growth of a normal fault. Below the elastic discontinuity, the main difference between reverse and normal faulting is that, in agreement with the maximum energy release criterion (Fig. 2), normal faulting promotes greater dip angles ($\delta \geq 45^\circ$) quickly reached after the crack growth starts.

In Fig. 7 for cases with $r < 1$, the fault growth is accomplished only assuming high pore pressures. According to our model, results for high fluid pore pressure $p(z)$ (Figs 7b and d) do not reproduce the ones with no friction (Fig. 6b) owing to the presence of elastic interactions between fault elements which do not depend on p ($f_d Y_{mk}$ terms in system 20).

Fig. S1 shows the results of other simulations that consider a lower friction coefficient in the deepest layer for both reverse and normal faults of SET4. In these cases, we assume that the layer with a lower rigidity and therefore a lower tectonic stress, has also lower friction coefficient ($f_d = 0.05$). This assumption allows the crack growth even in the presence of small tectonic stress and p (e.g. SIM16R to be compared to SIM15R with $p = p_f$ in Table 1). If we don't consider the friction lowering, the crack cannot even start its growth in the cases where layer 1 has both a low rigidity and low tectonic stress as for example in SIM15R and SIM15N ($r = 0.2$, with $p = p_f$, Table 1) unless a high fluid pore pressure is assumed (Figs 7b and d). The friction coefficient has an effect on the direction of crack growth as emphasized in SIM21R and SIM21N (Fig. S1, $r = 1$) that have a uniform rigidity along depth: in these cases the dip-angle change at the interface depends primarily on the change of the dynamic friction coefficient.

4 DISCUSSION AND CONCLUSIONS

In this work we implemented an iterative BEM model in order to simulate crack growth across a welded layered elastic medium. We started from an initial planar fault formed by 10 dislocation elements, embedded in a lithostatic stress field superimposed onto a horizontal tectonic stress. We initially compute the stress equilibrium with the BEM procedure (eqs 19 and 20), then we impose that the energy release is positive

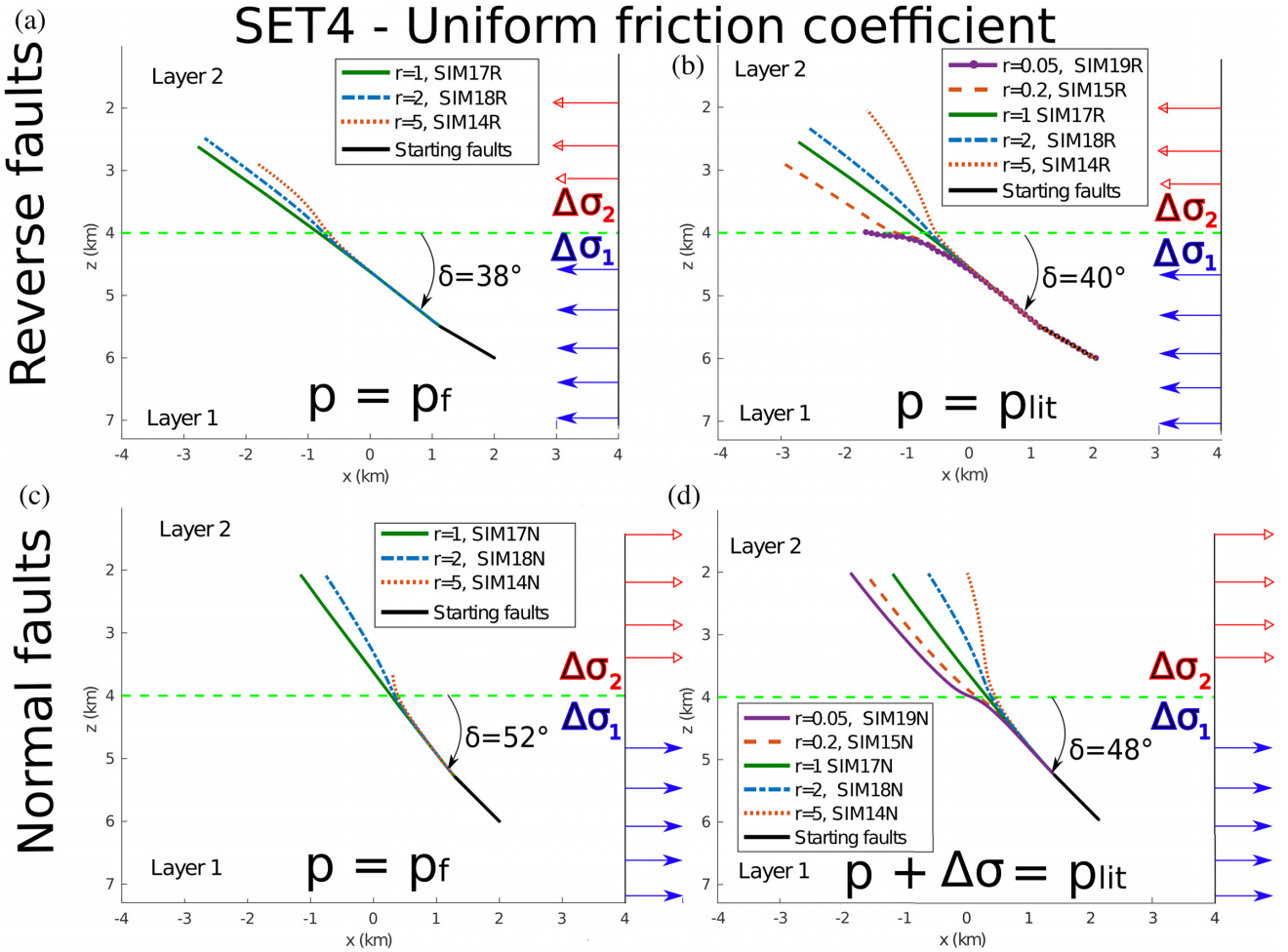

Figure 7. Crack growth pattern (coloured lines) obtained in simulations of SET4 (heterogeneous elastic medium, presence of friction). The tectonic stress $\Delta\sigma$ is rescaled according to the rigidity ratio r. The maximum values in magnitude are $\Delta\sigma = 0.06$ GPa for normal faults and $\Delta\sigma = -0.15$ GPa for reverse faults. The simulations have different rigidity ratios. Starting planar faults (black lines) have a dip-angle $\delta = 30°$ for reverse faults and $\delta = 45°$ for normal faults. The green dashed line shows the elastic discontinuity. Panels (a) and (c) show results for hydrostatic pore pressure, p_f, and $f_d = 0.3$ for a reverse (a) and a normal (c) fault. Panel (b) refers to a reverse fault with lithostatic pore pressure, p_{lit}, and panel (d) refers to a normal fault with a pore pressure equal to the lithostatic one minus $\Delta\sigma$.

in order to allow the crack growth and the maximum energy release to determine its direction. The growth of the crack has been simulated by iterative addition of dislocation elements, whose dip angles are chosen as to provide the greatest release of energy, which results in the minimum potential energy, in the spirit of Griffith's energy criterion of failure (Melosh & Williams 1989).

Preliminarily, we study the growth of cracks embedded in a homogeneous elastic medium with uniform tectonic stress without friction (SET1, Fig. 5) and we find that all cracks, regardless of the dip-angle of the initial fault plane, quickly bend to a dip-angle $\delta \approx 45°$ (the direction of maximum shear stress) and they maintain this direction indefinitely. In absence of friction, a dip-angle of 45° is provided both by the Anderson's theory of faulting (Anderson 1942) and by the maximum energy release criterion (eq. 12). While including friction both numerical and analytical results based on the maximum energy release criterion (Section 1.1) lead, respectively to a lower dip-angle for normal faults and a greater dip-angle for reverse faults with respect to the Anderson's theory (Figs 2 and 7). Dip angles of about 53° and 36° for normal and reverse faults, respectively, are predicted by the Anderson's theory for $f_s = 0.3$. Our results confirm that in a homogeneous medium ($r = 1$ and uniform friction), the fault does not bend (SIM17R and N in Fig 7).

Otherwise, when faults cross a rigidity contrast interface, they are affected by a dip angle change that increases in magnitude for larger rigidity contrasts. If $r > 1$ i.e. the fault starts in the medium with higher rigidity, rising towards the interface with the lower rigidity medium, it bends getting a greater dip angle up to become almost vertical (e.g. SIM6 and 7 in Fig. 6) or listric. On the contrary if $r < 1$, that is the fault starts in the medium with lower rigidity, rising towards the interface with the higher rigidity medium, it bends getting a smaller dip angle up to become almost horizontal (e.g. SIM5 and 9 in Fig. 6) or a detachment fault. This behaviour is due to the shear stress induced by deeper dislocation elements on the shallowest ones. Indeed, while in a homogeneous medium the maximum shear stress induced by a single dislocation element is along its dip-direction (Fig. S2d), the maximum shear stress in presence of a shallow layer with low rigidity ($r > 1$), is

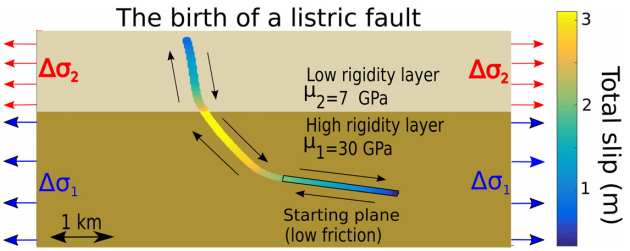

Figure 8. Crack growth pattern (coloured thick line) obtained in simulations of SET22N (heterogeneous elastic medium, presence of friction). The tectonic stress is $\Delta\boldsymbol{\sigma}_1 = 30$ MPa in the lower layer, while in the upper layer $\Delta\sigma_2 = \Delta\sigma_1 / r$ where $r = \mu_1/\mu_2$ (Table 1). The pore pressure is assumed as hydrostatic. The dynamic friction coefficient is $f_d = 0.3$ all over the fault surface apart from the starting low-dip segment (enclosed within a black rectangle) that has lower friction coefficient ($f_d = 0.05$). The colour represents the distribution of the total slip (or Burger's vector) magnitude occurred during all the crack (or fault) growth. Black arrows show the direction of slip.

obtained in a clockwise rotated direction with respect to the fault dip (Fig. S2e). Vice versa an anticlockwise rotation is fostered considering a crack that reaches a stiffer medium ($r < 1$, Fig. S2f).

According to Vendeville (1991) the mechanism generating fault curvature can be subdivided into two different groups: the first one assumes that curvature is due to a mechanical origin, mainly related to vertical changes in friction and/or stress field, the second one assumes that the curvature of the faults is induced as a result of their formation due to compaction and sedimentation. Vendeville (1991) also says that the dip changes introduced by the friction coefficient are minimal and could not explain, alone, great fault curvatures as confirmed also by experimental approaches (Vasquez *et al.* 2018). This is in accordance with our results in a homogeneous medium ($r = 1$), as evidenced by SIM21R and SIM21N in Figs S1 where the effect of friction variation on the fault geometry is modelled: the crack growth direction primarily depends on the fault mechanism and secondly on the dynamic friction coefficients, f_d. (Figs 7 and S1). The results of the present paper allow us to interpret several complexities of the dip-slip fault geometry in terms of rigidity contrasts.

4.1 Listric faults

A listric fault usually flattens downwards (Shelton 1984; Spahić *et al.* 2011) with a low-angle plane lying on a (as often assumed) undeformed basement (Mauduit & Brun 1998). Even if listric faults are more common in extensional environments (Maloney *et al.* 2012), they can also occur in compressional regimes (Groshong 2006). The synsedimentary listric faults are well documented by seismic data, as mainly described by reflection seismic surveys, but they are not restricted to these environments and may also involve crustal basement (Mandl 1988). An example of a normal listric fault is the Gubbio (central Italy) fault (Mirabella *et al.* 2004), while the high angle–dipping listric fault that led to the M_w 7.9 Wenchuan (China) earthquake of 12 May 2008 (Zhang *et al.* 2010) is a reverse fault. Also, the Laramide front of New Mexico (Magnani *et al.* 2013) is characterized by listric thrust faulting. The basal orientation of a listric fault plane is most likely favoured by the presence of deep mechanically weak layers and by pressurized fluids, which significantly reduce the effect of frictional resistance (Maloney *et al*. 2012; Passone & Mai 2017).

According to our model, listric geometries can be obtained only if $r > 1$, that is when the fault meets an interface above which the medium is softer. The results of simulations are quite stable and regardless of the dynamic friction coefficient, the magnitude of the tectonic stress, the pore pressure and the fault mechanism, the fault grows by increasing the dip angle in the shallow and less rigid layer. Nevertheless, it is worth to notice that if the tectonic stress decreases too much in the upper softer layer (case of uniform strain), and if the pore pressure is hydrostatic, the fault growth stops soon after crossing the interface (SIM14 in Figs 7a and c). This could provide an explanation to the formation of blind listric faults (e.g. fig. 3in Ekström *et al.* 1992).

An example of a $r > 1$ configuration is when shallow layers of recently formed sedimentary rocks, with low rigidity, are superimposed to stiffer layers whose rigidity increases with depth. This condition is very common as in the shallow and brittle crust, the rigidity generally increases with depth, as confirmed by depth-increasing *S*-wave speed, $V_s = \sqrt{\mu/\rho}$ (e.g. Haslinger *et al.* 1999; Nespoli *et al.* 2017, 2018) despite the density ρ is usually estimated to increase with depth. Then, the listric fault geometry is expected to be common according to our model. The rigidity contrast can be so effective on crack growth to bend the fault planes up to a dip-angle $\geq 45^\circ$ even in case of reverse faults (SIM14R, Figs 7a and b). In case of normal faults, the crack is allowed to propagate in the shallow softer layer almost vertically (SIM14N in Figs 7c and d to be compared with fig. 2 of Tung & Masterlark 2018).

Fig. 8 shows the results of SIM22N ($r > 1$, Table 1) that reproduces the crack growth of a typical listric fault. The starting plane was modelled with a larger width with respect to other simulations, a dip of 10° and a low dynamic friction ($f_d = 0.05$). Most of the slip released during all the crack growth occurs in the central segment of the fault. The low dynamic friction on the starting plane is needed in order to allow the crack to start its growth, which continues up to the surface by defining a clear listric geometry. In the next paragraph we will state the conditions promoting such a low angle starting plane.

4.2 Detachment and ramp-flat-ramp faults

Detachment faults (i.e. curved, convex-upward faults with decreasing dip at shallower depths) are envisaged to occur at ocean ridges and represent an important mechanism in the generation of the oceanic crust (Smith *et al.* 2006). Moreover, in ramp-flat-ramp structures the fault surface in characterized by high-dip segments connected by a low-dip segment. Detachments often derive from low-angle normal faults, but they also occur where thrusts move above a layer of a very weak and ductile material (Scholz 2002). Braunmiller & Nabelek (1996) assess that the formation of detachments can be justified below the schizosphere (i.e. below the brittle–ductile transition). In real cases, for low angle faults such as the Woodlark detachment fault (SW Pacific), the Corinth Rift detachment (Jolivet *et al*. 2010 and reference therein), the Altotiberina (Central Italy) fault (Collettini & Barchi 2002; Anderlini *et al.* 2016; Pauselli & Ranalli 2017) a vanishing frictional resistance is usually ascribed to their formation even if the problem is not completely resolved (Yue & Suppe 2014).

According to our results, detachment faults and ramp-flat-ramp faults can be realized only if $r < 1$ (Figs 6 and 7). Beside this condition, a low dynamic friction coefficient in the deeper layer (SIM16N and SIM16R in Fig. S1) or a high pore pressure (SIM15N and SIM15R in Fig. 7) is necessary at least if the strain is uniform along depth, as we definitely assumed in SET4. Otherwise, if friction is not low enough, the fault is even not able to start growing as in simulations SIM15, SIM19 and SIM20 unless a high pore pressure is considered (Figs 7b and d) because the energy release is not sufficient to provide the work dissipated by friction. Another way to allow crack growth with $r < 1$ in presence of friction could be to assume a tectonic stress uniform with depth (as in SET2) as due to the cumulative effect of previous earthquakes occurred in the stiffer layer.

Only if $r \ll 0.2$ (Fig. 6a) the fault can propagate along the elastic discontinuity producing the horizontal detachment of the deeper layer with respect to the shallower one (i.e. a decollement fault), without penetrating the upper stiffer layer. The decollement of SIM5 (Fig. 6a) cannot cross the stiffer layer since this is energetically disfavoured. Accordingly if r is equal to 20 per cent or larger some alternative mechanisms should be provided to model decollement faults [e.g. for normal faults, deflected stresses (Axen 1992) or mineralogical weakening (Smith & Faulkner 2010)]. It is worth to notice that, according to our model, we achieve a persistent horizontal crack growth only assuming a strong contrast ($r = 0.05$), a vanishing friction coefficient and a uniform stress along depth (SIM 5 in Fig. 6a), otherwise, if stress is proportional to rigidity, the fault is allowed to penetrate the upper medium (SIM9 in Fig 6b), forming a ramp-flat-ramp structure, as we will discuss below. Nevertheless, our results show that a high pore pressure can promote a fault growth with very low dip values (e.g. SIM19R and SIM19N, Figs 7b and d, respectively) in agreement with Hubbert & Rubbey (1959).

In the case $r = 0.05$ the interface above the much softer deeper layer might be identified with the brittle-ductile transition within the crust (SIM5 in Fig. 6a to be compared with Fig. 2b in Jolivet *et al*. 2010). Below this transition an elasto-plastic rock rheology can be assumed, where plasticity is realized if the deviatoric stress is above a threshold. In these conditions rocks behave like viscoelastic materials with very low viscosity and we can assume as a rough approximation an effective elastic behaviour with very low rigidity (e.g. Carcione *et al*. 2014), especially near the crack tip where deviatoric stresses concentrate. Usually detachments mark the brittle-ductile transition (e.g. Fayon *et al*. 2000; Jolivet *et al*. 2010; Platt *et al*. 2014; Rabillard *et al*. 2018) where they can be interpreted as ductile shear zones (Rabillard *et al*. 2018) also called ductile faults (Scholz 2002).

Ramp-flat-ramp faults usually occur in layered, large-scale, extensional environments (Fossen 2016) consisting of two high dip-angle ramps linked by a subhorizontal segment (flat). Some examples of ramp-flat-ramp faults are in the eastern Betic Cordillera, Spain (Pedrera *et al*. 2012), in the Norwegian Njord oil field (Ehrlich & Gabrielsen 2004) and in the Monte Amiata geothermal area in Italy (Brogi 2004). A ramp-flat-ramp fault growing almost horizontally in correspondence of the elastic discontinuity, and then allowed to rise in the stiffer layer after some iterations can be obtained for strong rigidity contrasts, low friction or high pore pressure if a vertically uniform strain is assumed in elastic medium (SIM9, Fig. 6b and SIM19N in Fig. 7 and 20 N in Fig. S1 to be compared with fig. 1 of Vasquez *et al*. 2018). It is worth to note that the higher the rigidity ratio r, the wider the flat (compare e.g. SIM9 to SIM12 in Fig. 6b or SIM20N to SIM16N in Fig. S1d) in agreement with experiments by Vasquez *et al*. (2018).

Our results reinforce the hypothesis that when faults grow at depth in low rigidity or ductile media, low-dipping faults, leading to the creation of detachment planes, are allowed by a combination of three factors: great contrasts of rigidity in which a layer with high rigidity is superimposed to the softer layer, a high pore pressure (Figs 7b and d and Figs S1b and d) or a low dynamic friction coefficient at least in the softer layer (Fig. S1, all cases).

4.3 Concluding remarks

We devised a quasi-static crack model for fault growth across a two welded elastic half-spaces, where the fault configuration at a given instant of time is interpreted as the cumulative effect of successive slip events. As we do not pre-assign the fault surface, we use the maximum energy release criterion to determine the orientation of the incremental surface during fault growth as a part of the solution.

This approach allows us to assess that the presence of crustal rigidity contrasts: (i) justifies non-Andersonian geometries characterized by high and low dip-angles in the case of reverse and normal faults, respectively and (ii) considerably influences the fault growth direction allowing to create curved fault surfaces: faults rising toward softer regions tend to become listric while faults rising towards stiffer regions tend to behave as detachments.

It might be interesting to extend our model to several layers with different rigidity or rheology, bounded by a free surface, in order to model a wider and more realistic range of cases. Even considering a two-layer configuration, following the criterion of maximum energy

release, our results suggest that significant changes of the dip angle can be obtained, strongly localized near the layer discontinuities, in both cases of extensive and compressive tectonic environments. This means that the rigidity contrast can foster the birth of a curved fault geometry and it is a key parameter for its interpretation.

ACKNOWLEDGEMENTS

We thank the anonymous reviewers whose comments and suggestions greatly improved our work.

REFERENCES

Anderlini, L., Serpelloni, E. & Belardinelli, M.E., 2016. Creep and locking of a low-angle normal fault: insights from the Altotiberina fault in the Northern Apennines (Italy), *Geophys. Res. Lett.,* **43,** 4321–4329.

Axen, G.J., 1992. Pore pressure, stress increase, and fault weakening inlow-angle normal faulting, *J. geophys. Res.,* **97,** 8979–8991.

Anderson, E.M., 1942, *The Dynamics of Faulting and Dyke Formation with Application to Britain,* Oliver & Boyd.

Baudon, C. & Cartwright, J.A., 2008. 3D seismic characterisation of an array of blind normal faults in the Levant Basin, eastern Mediterranean, *J. Struct. Geol.,* **30,** 746–760.

Bonafede, M. & Rivalta, E., 1999. The tensile dislocation problem in a layered elastic medium, *Geophys. J. Int.,* **136,** 341–356.

Braunmiller, J. & Nabelek, J., 1996. Geometry of continental normal faults: seismological constraints, *J. geophys. Res.,* **10,** 3045–3052

Brogi, A., 2004. Miocene low-angle detachments and upper crust mega boudinage in the Mt. Amiata geothermal area (Northern Apennines, Italy), *Geodinamica Acta,* **17**(6), 375–387.

Bürgmann, R. & Dresen, G., 2008. Rheology of the lower crust and upper mantle: evidence from rock mechanics, geodesy, and field observations, *Annu. Rev. Earth Planet. Sci.,* **36**(1), 531–567

Carcione, J.M., Poletto, F., Farina, B. & Craglietto, A., 2014. Simulation of seismic waves at the earth's crust (brittle–ductile transition) based on the Burgers model, *Solid Earth,* **5,** 1001–1010.

Célérier, B., 2008. Seeking Anderson's faulting in seismicity: a centennial celebration, *Rev. Geophys.,* **46,** RG4001, doi:10.1029/2007RG000240.

Chiarabba, C. & Amato, A., 2003. Vp and Vp/Vs images in the Mw 6.0 Colfiorito fault region (central Italy): a contribution to the understanding of seismotectonic and seismogenic processes, *J. geophys. Res.,* **108,** 2248, doi:10.1029/2001JB001665, B5.

Collettini, C. & Barchi, M.R., 2002. A low-angle normal fault in the Umbria region (Central Italy): a mechanical model for the related microseismicity, *Tectonophysics,* **359**(1–2), 97–115, ISSN 0040–1951.

Copley, A., 2017. The strength of earthquake-generating faults, *J. Geol. Soc.,* **175**(1), 1–12.

Convertito, V., Catalli, F. & Emolo, A., 2013. Combining stress transfer and source directivity: the case of the 2012 Emilia seismic sequence, *Sci. Rep.,* **3,** 3114, doi:10.1038/srep03114.

Cooke, M.L. & Murphy, S., 2004. Assessing the work budget and efficiency of fault systems using mechanical models, *J. geophys. Res.,* **109,** B10408, doi: 10.1029/2004JB002968.

Cowie, P.A. & Scholz, C.H., 1992. Growth of faults by accumulation of seismic slip, *J. geophys. Res.,* **97**(B7), 11 085–11 095.

Dahlen, F.A. & Tromp, J., 1998. *Theoretical Global Seismology,* xiv + 1025 pp., Princeton Univ. Press. ISBN 0 691 00116 2; 0 691 00124 3 (pb).

Du, Y. & Aydin, A., 1995. Shear fracture patterns and connectivity at geometric complexities along strike-slip faults, *J. geophys. Res.,* **100**(B9), 18 093–18 102.

Ehrlich, R. & Gabrielsen, R.H., 2004. The complexity of a ramp–flat–ramp fault and its effect on hanging-wall structuring: an example from the Njord oil field, offshore mid-Norway, *Pet. Geosci.,* **10**(4), 305–317.

Ekström, G., Stein, R.S., Eaton, J.P. & Eberhart-Phillips, D., 1992. Seismicity and geometry of a 110-km-long blind thrust fault 1. The 1985 Kettleman Hills, California, earthquake, *J. geophys. Res.,* **97**(B4), 4843–4864.

Erdogan, F. & Sih, G.C., 1963. On the crack extension in plates under plane loading and transverse shear, *J. Basic Eng.,* **85,** 519–525

Fayon, A.K., Peacock, S.M., Stump, E. & Reynolds, S.J., 2000. Fission track analysis of the footwall of the Catalina detachment fault, Arizona: tectonic denudation, magmatism, and erosion, *J. geophys. Res.,* **105**(B5), 11047–11062.

Ferrari, C. & Bonafede, M., 2012. Non-planar fault models: complexities induced by crustal layering in trascurrent faulting processes, *Geophys. J. Inter.,* **190,** 151–178.

Forsyth, D.W., 1992. Finite extension and low-angle normal faulting, *Geology,* **20**(1), 27–30.

Fossen, H., 2016. *Structural Geology,* 2nd edn, Cambridge Univ. Press, ISBN: 9781107057647.

Göldner, H., 1977. Sih, G.C. (Hrsg.), Methods of analysis and solutions of crack problems, A collection of solutions on stress intensity factors and strain energy-density factors, Leyden. Noordhoff International Publishing. 1973. 562 S., 220 Abb., Dfl. 144.25. $ 62.75 (Mechanics of fracture 1), *Z. Angew. Math. Mech.,* **57,** 497–497, doi:10.1002/zamm.19770570821.

Griffith, A., 1921. The phenomena of rupture and flow in solids, *Phil. Trans. R. Soc. Lond., A,* **221,** 163–198

Groshong, R.H., 2006. *3-D Structural Geology,* 2nd edn, Springer.

Gudmundsson, A., Guidi, G.D. & Scudero, S., 2013. Length–displacement scaling and fault growth, *Tectonophysics,* **608,** 1298–1309

Gunnars, J., Ståhle, P. & Wang, T., 1997. *Comput. Mech.,* **19,** 545, doi:10.1007/s004660050207.

Gupta, H.K., 2011. *Encyclopedia of Solid Earth Geophysics*. Springer, ISBN: 9789048187027, Doi:10.1007/978-90-481-8702-7.

Hainzl, S. & Fischer, T., 2002. Indications for a successively triggered rupture growth underlying the 2000 earthquake swarm in Vogtland/NW Bohemia, *J. geophys. Res.,* **107**(B12), 2338, doi:10.1029/2002JB001865.

Haslinger, F. *et al.*, 1999. 3D crustal structure from local earthquake tomography around the Gulf of Arta (Ionian region, NW Greece), *Tectonophysics,* **304**(3), 201–218, ISSN 0040–1951.

Hirano, S. & Yamashita, T., 2015. Dynamic antiplane rupture propagation crossing a material interface: modelling with BIEM, *Geophys. J. Int.,* **200**(2), 1222–1235.

Hubbert, M.K. & Rubey, W.W., 1959. Role of fluid pressure in mechanics of overthrust faulting: I. Mechanics or fluid-filled porous solids and its application to overthrust faulting, *Bull. geol. Soc. Am.,* **70**(2), 115–166.

Jackson, J.A., 1987. Active normal faulting and crustal extension, *Geol. Soc., Lond., Spec. Publ.,* **28,** 3–17, doi:10.1144/GSL.SP.1987.028.01.02.

Jaeger, J.C. & Cook, N.G.W., 1976. *Fundamentals of Rock Mechanics,* John Wiley.

Jolivet, L., Labrousse, L., Agard, P., Lacombe, O., Bailly, V., Lecomte, E., Mouthereau, F. & Mehl, C., 2010. Corinth Rifting and shallow-dipping detachments, clues from the Corinth Rift and the Aegean, *Tectonophysics,* **483,** 287–304.

Kame, N. & Yamashita, T., 1999. Simulation of the spontaneous growth of a dynamic crack without constraints on the crack tip path, *Geophys. J. Int.,* **139**(2), 345–358.

Kanamori, H. & Heaton, T.H., 2013. Microscopic and macroscopic physics of earthquakes, in *Geocomplexity and the Physics of Earthquakes,* eds Rundle, J.B. , Turcotte, D.L., & Klein, W., doi:10.1029/GM120p0147, AGU.

Kattenhorn, S. & Pollard, D., 1999. Is lithostatic loading important for the slip behavior and evolution of normal faults in the Earth's crust?, *J. geophys. Res.,* **104**(B12), 28 879–28 898.

Kostrov, V., 1974. Seismic moment and energy of earthquakes, and seismic flow of rock, *Phys. Solid Earth,* **1,** 13–21

Kusakabe, T. & Kame, N., 2017. Derivation of 2-D XBIEM kernels and their application to a rupture crossing a bimaterial interface, *Geophys. J. Int.,* **210**(3), 1374–1387.

Kusznir, N.J. & Park, R.G., 1984. The strength of intraplate lithosphere, *Phys. Earth planet. Inter.,* **36,** 224–235.

Logan, J.M., 1992. *The Influence of Fluid Flow on the Mechanical Behavior of Faults,* American Rock Mechanics Association.

Maccaferri, F., Bonafede, M. & Rivalta, E., 2010. A numerical model of dyke propagation in layered elastic media, *Geophys. J. Int.,* **180,** 1107–1123.

Magnani, M.B., Levander, A., Erslev, E.A., Bolay-Koenig, N. & Karlstrom, K.E., 2013. Listric thrust faulting in the Laramide Front of North-Central New Mexico Guided by Precambrian basement structures, in *The Rocky Mountain Region: An Evolving Lithosphere,* eds Kalstrom, K.E. & Keller, G.R., doi:10.1029/154GM17, AGU.

Maloney, D., Davies, R., Imber, J. & King, S., 2012. Structure of the footwall of a listric fault system revealed by 3D seismic data from the Niger Delta, *Basin Res.,* **24,** 107–123.

Mandl, G., 1988. *Mechanics of Tectonic Faulting: Models and Basic Concepts,* Elsevier.

Mauduit, T. & Brun, J.P., 1998. Growth fault/rollover systems: birth, growth, and decay, *J. geophys. Res.,* **103**(B8), 18 119–18 136.

McBeck, J.A., Cooke, M.L., Herbert, J.W., Maillot, B. & Souloumiac, P., 2017. Work optimization predicts accretionary faulting: an integration of physical and numerical experiments, *J. geophys. Res.,* **122,** 7485–7505.

McBeck, J., Cooke, M., Souloumiac, P., Maillot, B. & Mary, B., 2018. The influence of detachment strength on the evolving deformational energy budget of physical accretionary prisms, *Solid Earth,* **9,** 1421–1436.

McGarr, A. & Gay, N.C., 1978. State of stress in the Earth'scrust, *Annu. Rev. Earth planet. Sci.,* **6,** 405–436.

Melosh, H.J. & Williams, C.A., 1989. Mechanics of graben formation in crustal rocks: a finite element analysis, *J. geophys. Res.,* **94**(B10), 13 961–13 973.

Mirabella, F., Ciaccio, M.G., Barchi, M.R. & Merlini, S., 2004. The Gubbio normal fault (Central Italy): geometry, displacement distribution and tectonic evolution, *J. Struct. Geol.,* **26**(12), 2233–2249.

Mohapatra, G.K. & Johnson, R.A., 1998. Localization of listric faults at thrust fault ramps beneath the Great Salt Lake Basin, Utah: evidence from seismic imaging and finite element modeling, *J. geophys. Res.,* **103**(B5), 10 047–10 063.

Mulargia, F., Castellaro, S. & Ciccotti, M., 2004. Earthquakes as three stage processes, *Geophys. J. Int.,* **158,** 98–108.

Nalbant, S.S., Steacy, S., Sieh, K., Natawidjaja, D. & McCloskey, J., 2005. Earthquake risk on the Sunda trench, *Nature,* **435,** 756–757.

Nespoli, M., Belardinelli, M.E., Anderlini, L., Bonafede, M., Pezzo, G., Todesco, M. & Rinadli, A.P., 2017. Effects of layered crust on the coseismic slip inversion and related CFF variations: hints from the 2012 Emilia Romagna earthquake, *Phys. Earth planet. Inter.,* **273,** 23–35.

Nespoli, M., Belardinelli, M.E., Gualandi, A., Serpelloni, E. & Bonafede, M., 2018. Poroelasticity and fluid flow modeling for the 2012 Emilia-Romagna earthquakes: hints from GPS and InSAR data, *Geofluids,* **2018** , doi:10.1155/2018/4160570.

Okubo, C.H. & Schultz, R.A., 2005. Evolution of damage zone geometry and intensity in porous sandstone: insight gained from strain energy density, *J. Geol. Soc.,* **162,** 939–949.

Olson, E.L. & Cooke, M.L., 2005. Application of three fault growth criteria to the Puente Hills thrust system, Los Angeles, California, USA, *J. Struct. Geol.,* **27**(10), 1765–1777.

Passone, L. & Mai, P.M., 2017. Kinematic earthquake ground-motion simulations on listric normal faults, *Bull. seism. Soc. Am.,* **107**(6), 2980–2993.

Pauselli, C. & Ranalli, G., 2017. Effects of lateral variations of crustal rheology on the occurrence of post-orogenic normal faults: the Alto Tiberina Fault (northern Apennines, Central Italy), *Tectonophysics,* **721,** 45–55.

Pedrera, A., Galindo-Zaldívar, J., Lamas, F. & Ruiz-Constán, A., 2012. Evolution of near-surface ramp-flat-ramp normal faults and implication during intramontane basin formation in the eastern Betic Cordillera (the Huércal-Overa Basin, SE Spain), *Tectonics,* **31,** TC4024, doi: 10.1029/2012TC003130.

Platt, J.P., Behr, W.M. & Cooper, F.J., 2014. Metamorphic core complexes: windows into the mechanics and rheology of the crust, *J. Geol. Soc.,* **172,** 9–27.

Pollard, D.D. & Fletcher, R.C., 2005. *Fundamentals of Structural Geology,* Cambridge Univ. Press.

Rabillard, A., Jolivet, L., Arbaret, L., Bessière, E., Laurent, V., Menant, A., Augier, R. & Beaudoin, A., 2018. Synextensional granitoids and detachment systems within Cycladic metamorphic core complexes (Aegean Sea, Greece): toward a regional tectonomagmatic model, *Tectonics,* **37,** 2328–2362.

Rivalta, E., Mangiavillano, W. & Bonafede, M., 2002. The edge dislocation problem in a layered elastic medium, *Geophys. J. Int.,* **149**(2), 508–523.

Scholz, C., 2002. *The Mechanics of Earthquake Faulting,* 2nd edn, Cambridge Univ. Press, doi:10.1017/CBO9780511818516, ISBN 0521655404.

Selcuk, S., Hurd, D.S., Crouch, S.L. & Gerberich, W.W., 1994. Prediction of interfacial crack path: a direct boundary integral approach and experimental study, *Int. J. Fract.,* **67,** 1–20.

Shelton, W.J., 1984. Listric normal faults, an illustrated summary, *Am. Assoc. Petrol. Geol. Bull.,* **68,** 801–815

Sibson, R.H., 1990. Conditions for fault-valve behavior, *Geol. Soc., Lond., Speci. Publ.,* **54,** 15–28.

Smith, D.K., Cann, J.R. & Escartin, J., 2006. Widespread active detachment faulting and core complex formation near 138 N on the Mid Atlantic, *Nature,* **442,** 440–443.

Smith, S.A.F. & Faulkner, D.R., 2010. Laboratory measurements of the frictional properties of the Zuccale low-angle normal fault, Elba Island, Italy, *J. geophys. Res.,* **115,** B02407, doi:10.1029/2008JB006274.

Spahić, D., Exner, U., Behm, M., Grasemann, B., Haring, A. & Pretsch, H., 2011. Listric versus planar normal fault geometry: an example from the Eisenstadt-Sopron Basin (E Austria), *Int. J. Earth Sci. (GeolRundsch),* **100,** 1685, doi:10.1007/s00531-010-0583-5.

Stein, S. & Wysession, M., 2003. *An Introduction to Seismology, Earthquakes, and Earth Structure,* pp. 512, Blackwell Publishing, ISBN 0-865-42078-5.

Tallarico, A., Santini, S. & Dragoni, M., 2005. Stress changes due to recent seismic events in the Central Apennines (Italy), *Pure appl. Geophys.,* **162,** 2273–2298.

Thio, H.K., 2009. Earthquake mechanics in geophysics and geochemistry, Volume II, [Ed. Jan Laštovicka], in *Encyclopedia of Life Support Systems (EOLSS), Developed under the Auspices of UNESCO,* Eolss Publishers.

Tung, S. & Masterlark, T., 2018. Resolving source geometry of the 24 August 2016 Amatrice, Central Italy, earthquake from InSAR Data and 3D finite-element modeling, *Bull. seism. Soc. Am.,* **108**(2), 553–572.

Turcotte, D. & Schubert, G., 2002. *Geodynamics,* 2nd edn, Cambridge Univ. Press, ISBN 1107268672, 9781107268678.

Vasquez, L., Nalpas, T., Ballard, J.-F., De Veslud, C.L.C., Simon, B., Dauteuil, O. & Du Bernard, X., 2018. 3D geometries of normal faults in a brittle-ductile sedimentary cover: analogue modelling, *J. Struct. Geol.,* **112,** 29–38.

Vendeville, B., 1991. Mechanisms generating normal fault curvature: a review illustrated by physical models, *Geol. Soc., Lond., Spec. Publ.,* **56,** 241–249.

Voight, B., 1976. *Mechanics of Thrust Faults and Decollements,* Dowden, Huchinson, and Ross.

Wernicke, B., 1995. Low-angle normal faults and seismicity: a review, *J. geophys. Res.,* **100**(B10), 20 159–20 174.

Yagupsky, D.L., Brooks, B.A., Whipple, K., Duncan, C.C. & Bevis, M., 2014. Distribution of active faulting along orogenic wedges: minimum-work models and natural analogue, *J. Struct. Geol.,* **66,** 237–247.

Yue, L.F. & Suppe, J., 2014, Regional pore-fluid pressures in the active western Taiwan thrust belt: a test of the classic Hubbert–Rubey fault-weakening hypothesis, *J. Struct. Geol.,* **69,** 493–518.

Zhang, P.-Z., Wen, X.-Z., Shen, Z.-K. & Chen, J.-H., 2010. Oblique, high-angle, listric-reverse faulting and associated development of strain: the Wenchuan earthquake of May 12, 2008, Sichuan, China, *Annu. Rev. Earth planet. Sci.,* **38,** 351–380

SUPPORTING INFORMATION

Supplementary data are available at *GJI* online.

Figure S1. Crack growth pattern (coloured lines) obtained in simulations of SET4 (heterogeneous elastic medium, presence of friction). The tectonic stress in the upper layer is $\Delta\sigma_2 = 60$ MPa (–150 MPa) for normal (reverse) faults, while in the lower layer is rescaled according to the rigidity ratio r (indicated in labels). Starting planar faults (black lines) have a dip-angle $\delta = 30^\circ$ for reverse faults and 45° for normal faults. The green dashed line represents the elastic discontinuity. The fault surface is characterized by different friction coefficients, according to its depth: within the upper layer $f_d = 0.3$, while in the deepest layer $f_d = 0.05$. Panel (a) and (c) refer to a reverse and normal fault, respectively for hydrostatic pore pressure p. Panel (b) refers to a reverse and normal fault, for lithostatic pore pressure, while panel (d) refers to a normal fault with the maximum possible value of pore pressure.

Figure S2. Induced shear stress (a, b and c) and induced maximum shear stress (d, e and f) generated by a reverse dislocation (yellow segment) with $b = 1\ m$, $f_s = 0.4$ and $\delta = 30^\circ$ in a layered medium. The green dashed line represents the elastic discontinuity. Shear stress is computed considering a receiving fault with the same dip as the dislocation source. The homogeneous medium (a, d) has a rigidity $\mu = 30$ GPa and a Poisson's modulus $\nu = 0.25$. Indicating with μ_1 the rigidity of the deeper layer and μ_2 the rigidity of the shallower one, in panels (b) and (e) $\mu_1 = 30$ GPa and $\mu_2 = 6$ GPa, while in panels C and F, $\mu_1 = 6$ GPa and $\mu_2 = 30$ GPa. The Poisson ratio is $\nu = 0.25$ everywhere. Colour and contour represent stresses magnitude expressed in MPa. The magenta rectangles in panels (a), (b) and (c) delimit the area represented in panels (d), (e) and (f). Yellow and grey bars show the orientation of the planes of maximum shear stress.